

# The Angular Size Distribution of $\mu\text{Jy}$ Radio Sources

W. D. Cotton<sup>1</sup>, J. J. Condon<sup>1</sup>, K. I. Kellermann<sup>1</sup>, M. Lacy<sup>1</sup>, R. A. Perley<sup>2</sup>,  
A. M. Matthews<sup>3</sup>, T. Vernstrom<sup>4</sup>, Douglas Scott<sup>5</sup>, J. V. Wall<sup>5</sup>

<sup>1</sup>*National Radio Astronomy Observatory, 520 Edgemont Road, Charlottesville, VA 22903, USA*

<sup>2</sup>*National Radio Astronomy Observatory, P.O. Box 0, Socorro, NM 87801, USA*

<sup>3</sup>*Astronomy Department, University of Virginia, Charlottesville, VA, USA*

<sup>4</sup>*Dunlap Institute for Astronomy and Astrophysics, University of Toronto, Toronto, ON M5S 3H4 Canada*

<sup>5</sup>*Department of Physics and Astronomy, University of British Columbia, Vancouver, BC V6T 1Z1, Canada*

## ABSTRACT

We made two new sensitive (rms noise  $\sigma_n \approx 1 \mu\text{Jy beam}^{-1}$ ) high resolution ( $\theta = 3''0$  and  $\theta = 0''.66$  FWHM) S-band ( $2 < \nu < 4$  GHz) images covering a single JVLA primary beam (FWHM  $\approx 14'$ ) centered on J2000  $\alpha = 10^{\text{h}} 46^{\text{m}}$ ,  $\delta = +59^\circ 01'$  in the Lockman Hole. These images yielded a catalog of 792 radio sources,  $97.7 \pm 0.8\%$  of which have infrared counterparts stronger than  $S \approx 2 \mu\text{Jy}$  at  $\lambda = 4.5 \mu\text{m}$ . About 91% of the radio sources found in our previously published, comparably sensitive low resolution ( $\theta = 8''$  FWHM) image covering the same area were also detected at  $0''.66$  resolution, so most radio sources with  $S(3 \text{ GHz}) \gtrsim 5 \mu\text{Jy}$  have angular structure  $\phi \lesssim 0''.66$ . The ratios of peak brightness in the  $0''.66$  and  $3''$  images have a distribution indicating that most  $\mu\text{Jy}$  radio sources are quite compact, with a median Gaussian angular diameter  $\langle \phi \rangle = 0''.3 \pm 0''.1$  FWHM and an rms scatter  $\sigma_\phi \lesssim 0''.3$  of individual sizes. Most of our  $\mu\text{Jy}$  radio sources obey the tight far-infrared/radio correlation, indicating that they are powered by star formation. The median effective angular radius enclosing half the light emitted by an exponential disk is  $\langle \rho_e \rangle \approx \langle \phi \rangle / 2.43 \approx 0''.12$ , so the median effective radius of star-forming galaxies at redshifts  $z \sim 1$  is  $\langle r_e \rangle \approx 1.0$  kpc.

*Subject headings:* catalogs — galaxies: fundamental parameters — galaxies: star formation — infrared: galaxies — radio continuum: galaxies — surveys

## 1. Introduction

We recently reported the results of a low-resolution ( $\theta = 8''$  FWHM) S-band ( $2 < \nu < 4$  GHz) image made with the NRAO<sup>1</sup> Karl G. Jansky Very Large Array (VLA) C configuration, covering a single primary beam (FWHM  $\approx 14'$ ) centered on J2000  $\alpha = 10^{\text{h}} 46^{\text{m}}$ ,  $\delta = +59^\circ 01'$  in the Lockman Hole (Condon et al. 2012; Vernstrom et al. 2014). The rms noise and confusion in this image are comparable:  $\sigma_n \approx \sigma_c \approx 1 \mu\text{Jy beam}^{-1}$ . The rapidly falling Euclidean-normalized differential source count  $S^{5/2}n(S)$  at

$\mu\text{Jy}$  levels obtained from the confusion amplitude or “ $P(D)$ ” distribution, converted to 1.4 GHz via the median spectral index  $\langle \alpha \rangle = -0.7$ , closely follows predictions of evolutionary models (Condon 1984; Wilman et al. 2008) in which most  $\mu\text{Jy}$  radio sources are powered by recent star formation in galaxies at median redshift  $\langle z \rangle \sim 1$ .

Our  $\mu\text{Jy}$  source count is much lower than that of Owen & Morrison (2008), who derived a nearly constant  $S^{5/2}n(S)$  from their sensitive 1.4 GHz VLA image made at the same position with  $\theta = 1''.6$  resolution. Owen & Morrison (2008) corrected their source count for the effects of partial resolution using a source angular-size distribution with median FWHM  $\langle \phi \rangle \approx 1''.2$  and a tail extending to much larger angular sizes.

<sup>1</sup>The National Radio Astronomy Observatory is a facility of the National Science Foundation operated under cooperative agreement by Associated Universities, Inc.

Condon et al. (2012) detected all of the overlapping Owen & Morrison (2008) sources, so it appears that the count correction required by the broad source angular-size distribution used is the primary cause of the higher Owen & Morrison (2008) source count. A steep differential source count  $n(S) \propto S^{-5/2}$  magnifies the impact of over-estimated angular sizes on count corrections. A similar effect has appeared in numerous published source counts at sub-mJy levels, all of which were corrected for a range of assumed angular-size distributions and consequently disagree by amounts far greater than the published uncertainties (Condon 2007; Heywood et al. 2013).

F. Owen (private communication) recently made a sensitive VLA 1.5 GHz image ( $\theta = 1''.6$  resolution,  $\sigma = 2.2 \mu\text{Jy beam}^{-1}$  rms noise) of the GOODS-N field and found a typical FWHM source size  $\langle\phi\rangle \sim 1''$ . However, this result depends on data from a single VLA configuration and does not include multi-configuration images made with different VLA configurations and include tests using simulated data (of the type presented in Section 8) to demonstrate that the techniques used can robustly recover source sizes near or slightly below the instrumental resolution.

A sensitive high-resolution ( $\theta \approx 0''.22$ ) survey of the GOODS-N field using the VLA at 10 GHz (Murphy et al. 2017) recently detected a sample of 32 sources with a much smaller median angular diameter  $\langle\phi\rangle = 0''.167 \pm 0''.032$  and rms size scatter  $\sigma_\phi \approx 0''.091$ . Radio sources in star-forming galaxies are expected to be smaller at 10 GHz, owing to the stronger contribution of free-free emission, while the synchrotron radiation dominating at lower frequencies is spread out by cosmic-ray diffusion. However, the cosmic-ray diffusion is too small to grow sources from  $0''.17$  at 10 GHz to  $1''$  at 1.5 GHz. Thus, there is still a significant spread in the reported median angular diameters of  $\mu\text{Jy}$  radio sources, and they remain disturbingly correlated with the resolution of the images used to find and fit Gaussians to the sources.

We believe that previous attempts to measure angular-size distributions and counts of faint radio sources have disagreed largely because: (1) they depended on sensitive images made with only a single high-resolution antenna configuration; (2) high-resolution images miss extended radio emission whose surface brightness is below the detec-

tion limit at that resolution; and (3) image noise tends to broaden Gaussians fitted to faint point sources by amounts proportional to the image resolution  $\theta$ . A more reliable method for constraining the angular-size distributions of source populations is to measure the peak flux densities (so-called “peak flux densities” are actually specific intensities written in units of flux density per beam solid angle; e.g.,  $\mu\text{Jy beam}^{-1}$ ) in two or more images made with different array configurations, yielding different angular resolutions but similar point-source sensitivities. See Appendices B and C of Murphy et al. (2017) for a discussion of this method.

This paper presents two new S-band images made with  $\theta = 3''.0$  and  $\theta = 0''.66$  resolution from VLA B- and A-configuration data, respectively. Both are centered on J2000  $\alpha = 10^{\text{h}} 46^{\text{m}}$ ,  $\delta = +59^\circ 01'$ . Extensive optical and infrared (IR) material on this field is available from Strazzullo et al. (2010), Mauduit et al. (2012), and Oliver et al. (2012). Both images have  $\sigma_n \approx 1 \mu\text{Jy beam}^{-1}$  rms noise and negligible confusion. The new  $3''$  and earlier  $8''$  images yield accurate total flux densities because they do not resolve the vast majority of the  $\mu\text{Jy}$  source population, while the  $\theta = 0''.66$  image should marginally resolve the  $\phi \lesssim 0''.5$  sources expected in the star-forming galaxies at redshifts  $z \sim 1$  that dominate the  $\mu\text{Jy}$  source population (Condon 1984; Wilman et al. 2008).

An initial analysis of the source population found in our  $8''$  resolution image was given in Vernstrom et al. (2016), who reported 10% radio-loud active galactic nuclei (AGNs), 28% radio-quiet AGNs, 58% star-forming galaxies, and 4% that could not be classified. Vernstrom et al. (2016) also gave a traditional discrete source count that needed little correction for partial resolution and agrees well with the deeper  $P(D)$  analysis.

## 2. Observations

The dates and durations of our sensitive VLA S-band observations centered on J2000  $\alpha = 10^{\text{h}} 46^{\text{m}}$ ,  $\delta = +59^\circ 01'$  are summarized in Table 1. The C-configuration observations were described in Condon et al. (2012), Vernstrom et al. (2014), and Vernstrom et al. (2016). The “B+” data were taken in the BnA configuration and during the

transition to A configuration, but they had insufficient temporal or frequency resolution for the longer BnA baselines to be used in our highest-resolution ( $\theta = 0''.66$ ) A-configuration image.

The new A-configuration data have higher frequency resolution (500 kHz) and were recorded with shorter (1 s) basic integration times to minimize bandwidth- and time-smearing within the half-power circle of the VLA primary beam. The VLA correlator also separated the observed frequency range  $1.989 \leq \nu$  (GHz)  $\leq 4.013$  into 16 contiguous subbands of width  $\Delta\nu = 128$  MHz each. The A-configuration data processing was similar to that described in Condon et al. (2012). Our flux-density calibration is based on a standard spectrum and model of 3C147 (Perley & Butler 2013a) and was transferred to the unresolved phase calibrator J1035+5628, whose absolute position uncertainty is  $< 0''.002$ . We used J1035+5628 to determine instrumental polarization and 3C147 (Perley & Butler 2013b) to calibrate the cross-polarized delays and phases. Calibration and editing used standard scripts in the Obit package (Cotton 2009)<sup>2</sup>. After calibration and extensive editing, the data were averaged over baseline-dependent time intervals chosen to minimize the size of the  $(u, v)$  data set but avoid time smearing.

### 3. Imaging

We imaged the data sets using a joint multi-frequency CLEAN that both minimizes frequency dependent effects and exploits the full sensitivity of the wideband data. A single-resolution CLEAN was adequate for this field dominated by nearly unresolved sources. The low resolution image was imaged and restored using a  $3''$  FWHM round, Gaussian beam and the high resolution data with a  $0''.66$  FWHM round, Gaussian beam. These values correspond to the resolution near the bottom of the ( $2 < \nu < 4$  GHz) band. Briggs' "optimal robust" weighting was used in the image formation (Briggs 1995).

<sup>2</sup>Obit software and documentation are available from <http://www.cv.nrao.edu/~simonbcotton/Obit.html>.

#### 3.1. Wide-band, Wide-field Imaging

The large fractional bandwidth and wide field-of-view that was imaged require that both the source spectra and the antenna gain as a function of position and frequency be taken into account. This was done by the Obit task MFImage, which divides the observed spectrum into frequency bins narrow enough that the variations in antenna gain and spectral differences among sources are small within each bin. For this purpose, we set the frequency bin width equal to the 128 MHz correlator subband width.

The image was divided into a large number of small facet planes to minimize the effects of sky curvature. The facets were reprojected onto a common tangent plane and grid to allow parallel CLEANing. A frequency-dependent  $(u, v)$  taper was applied to keep the angular resolution of the dirty beam the same in all frequency bins. This, plus the use of a single restoring beam, yields a meaningful 16-channel spectrum in each spatial pixel of the image cube.

For each major cycle of CLEAN, dirty and residual images were computed separately for each of the 16 frequency bins. The more sensitive full-bandwidth image, derived from the  $\sigma_i^{-2}$  noise-weighted average of the frequency-bin images, was used to drive the minor cycle CLEANing. The sensitive combined image and the combined dirty beam were used to locate new CLEAN components, and the dirty beam for the corresponding frequency bin and facet was used to derive the residuals for the next minor cycle.

Once the minor cycles hit their stopping criteria, the accumulated CLEAN model was subtracted from the visibility data. The CLEAN model subtracted from each frequency bin used the CLEAN flux density of each component in that bin corrected in frequency by the spectral index fitted to each component using all frequency bins. This process was accelerated by a Graphics Processing Unit (GPU).

After the CLEANing was done, the image in each frequency bin was restored with the components subtracted from that bin convolved with the single Gaussian restoring beam fitted to the central facet of the combined full-sensitivity image.

This procedure accommodates variations with frequency of antenna gain and source flux den-

sity by using frequency bins sufficiently narrow that variations within a bin do not disturb the image quality. The spectrum in a given pixel depends on both antenna gain and source spectral index. The antenna gain as a function of position and frequency was measured independently (Perley 2016), allowing the spectral indices of sufficiently strong sources to be determined. For weaker sources, we used the average spectral index  $\langle\alpha\rangle = -0.7$  to fit the source flux density at any frequency. That approximation is valid for most  $\mu\text{Jy}$  sources at S band.

Faraday rotation in the Stokes  $Q$  and  $U$  images is preserved if the frequency bins are sufficiently narrow and the rotation measure is not too large. A rotation measure  $\text{RM} = \pm 2000 \text{ rad m}^{-2}$  rotates the polarization position angle by  $1/2$  turn across a 128 MHz frequency bin at  $\nu \approx 3 \text{ GHz}$ , so larger RMs than this will cause significant Faraday depolarization.

### 3.2. CLEAN Windows

CLEAN deconvolution works best if it is constrained to place components only in spatial “windows” containing actual emission. Our CLEAN windows were generated or updated at the beginning of each major cycle by the combined (wide-band) image covering each facet. If the maximum residual lay outside the current window and its peak was higher than 5 times the facet rms, a new round window was added to the existing CLEAN window at the location of the peak, with a radius derived from the structure function about the peak. This allows CLEANing down to (or into) the noise and captures the bulk of the emission in the CLEAN model without producing excessive CLEAN bias.

### 3.3. Self-calibration

A single phase self-calibration was applied to the data. The model visibilities were calculated as was done in the CLEAN major cycles, and an independent phase solution was determined for each 10 minutes in each spectral window and polarization. These phases were interpolated in time and applied to all data.

### 3.4. Image Adjustments

The resulting images are 16 spectral-channel cubes covering  $2 < \nu(\text{GHz}) < 4$  that were jointly deconvolved and restored with a common spatial resolution. The sky brightness  $S_p(x, y)$  of the pixel offset by  $(x, y)$  from the pointing center at the reference frequency  $\nu_0 = 3 \text{ GHz}$  was calculated from the noise-weighted average of the spectral-window images:

$$S_p(x, y) = \frac{\sum_{i=1}^{16} \frac{S_i(x, y) \exp[-\alpha \ln(\nu_i/\nu_0)] g_i^2(x, y)}{g_i(x, y)}}{\sum_{i=1}^{16} \frac{g_i^2(x, y)}{\sigma_i^2}}, \quad (1)$$

where  $S_i(x, y)$  is the image (not corrected for primary-beam attenuation) brightness at pixel position  $(x, y)$  in spectral channel  $i$ ,  $\alpha \approx -0.7$  is the median source spectral index,  $\nu_i$  is the central frequency of spectral channel  $i$ ,  $0 \leq g_i(x, y) \leq 1$  is the normalized antenna gain at offset  $(x, y)$  from the pointing center and frequency  $\nu_i$ , and  $\sigma_i^2$  is the mean variance of source-free regions in the  $i$ th spectral image. The first factor in the numerator of Equation 1 corrects the bin brightness  $S_i(x, y)$  to the reference frequency using spectral index  $\alpha$  and divides it by the primary attenuation  $g_i(x, y)$  to yield the brightness on the sky  $S_p(x, y)$ . The second factor is the pixel weight that maximizes the signal-to-noise ratio, specifically the antenna gain  $g_i^2(x, y)$  divided by the spectral-channel image variance  $\sigma_i^2$ .

We approximated the normalized VLA antenna power gain  $g_i(x, y)$  by the theoretical gain of a uniformly illuminated circular aperture:

$$g_i(\rho) = \text{jinc}^2(D\rho/\lambda_i) \equiv \left[ \frac{2J_1(\pi D\rho/\lambda_i)}{\pi D\rho/\lambda_i} \right]^2, \quad (2)$$

where  $\rho = (x^2 + y^2)^{1/2}$  is the offset from the pointing center in radians,  $J_1$  is the Bessel function of the first kind of order 1 (Bracewell 2012),  $D = 25 \text{ m}$  is the aperture diameter, and  $\lambda_i = c/\nu_i$  is the wavelength at the center frequency  $\nu_i$  of spectral channel  $i$ . Equation 2 yields the primary beam FWHM  $\theta_{1/2}$  in practical units; it is

$$\left( \frac{\theta_{1/2}}{\text{arcmin}} \right) \approx 42.0 \left( \frac{\text{GHz}}{\nu} \right), \quad (3)$$

which is only  $\sim 1\%$  wider than the average beamwidth measured across S band (Perley 2016).

Applying Equation 1 corrects source flux densities for antenna gain but causes the image noise to increase radially as  $g_0^{-1}(\rho)$  away from the pointing center. In order to determine meaningful noise statistics in the neighborhood of each source, we multiplied the gain-corrected image by the antenna gain  $g_0(x, y)$  at the reference frequency  $\nu_0 = 3$  GHz during source finding and fitting. For example, our  $0''.66$  resolution A-configuration image extends to a radius  $\rho = 8'.3$ . After multiplication by  $g_0(\rho)$ , its mean off-source rms is  $\sigma = 0.96 \mu\text{Jy beam}^{-1}$ .

We made a comparable image with  $3''$  resolution and radius  $\rho = 13'.8$  using the combined uv-data from the longer C-configuration baselines and the shorter BnA-configuration baselines (Table 1). Additionally, we convolved the A-configuration image to  $3''$  resolution. Differences in celestial position and flux density scale of the two images were determined from the “at most” marginally resolved sources brighter than  $100 \mu\text{Jy beam}^{-1}$ . Finally, the B+C-configuration  $3''$  image was shifted in position ( $0''.006$  in  $\alpha$  and  $-0''.079$  in  $\delta$ ) and scaled in flux density (0.933) to agree with the  $3''$  A-configuration smoothed image, and the two  $3''$  images were weighted by  $\sigma^{-2}$  and combined. The differences in calibration are likely due to the extended period over which the B+C data were taken and the difficulties of calibration in a fierce RFI environment. The rms of the B+C image prior to primary beam correction was  $1.27 \mu\text{Jy beam}^{-1}$  and for the A-configuration image convolved to  $3''$  was  $1.88 \mu\text{Jy beam}^{-1}$ , giving relative weights of 70% and 30% respectively. Source-free regions in the final combined  $3''$  image have rms  $\sigma = 1.01 \mu\text{Jy beam}^{-1}$  prior to primary beam correction.

The  $3''$  resolution image has imaging artifacts near the strongest source in the field, a hot spot in the lobe of an FR II source. To avoid contaminating the image statistics, we masked these artifacts by assigning affected pixels a value indicating that they should be ignored in subsequent analysis.

#### 4. Radio Source Catalog

The Orbit task FndSou was used to generate two independent lists of radio components from the wideband  $\theta = 3''$  and  $\theta = 0''.66$  images, uncorrected for primary beam attenuation. Fnd-

Sou locates “islands” of contiguous pixels brighter than a chosen peak flux density threshold and fits one or more elliptical Gaussian components to the emission in each island. These fits are subject to a number of constraints; in particular, any fitted Gaussian narrower than the (circular) CLEAN restoring beam is unphysical and was fitted by a Gaussian at least as wide as the restoring beam.

FndSou initially fits Gaussians in one island at a time and ignores overlapping components in adjacent islands. After the first component list for each image was generated, the parameters of potentially overlapping components were reconciled by refitting them jointly with all other components lying within 25 pixels ( $2''.3$  on the  $\theta = 0''.66$  image or  $11''.0$  on the  $\theta = 3''$  image) in both  $\alpha$  and  $\delta$ . The sky peak flux density  $S_p$  ( $S_p^L$  for  $\theta = 3''$  and  $S_p^H$  for  $\theta = 0''.66$ ) of each Gaussian component was obtained by interpolating between image pixels to its fitted centroid position and dividing by the 3 GHz primary attenuation  $g_0$  at that position. Interpolations used the Lagrangian technique with a  $5 \times 5$  kernel. Resolved sources represented by multiple components were replaced by only the component closest to the IR galaxy position; these six sources are discussed further in Section 11.

The component lists from the  $\theta = 0''.66$  and  $\theta = 3''$  images were merged to form a single list of source candidates lying inside the circle with 3 GHz primary attenuation  $g_0 > 0.25$  (radius  $10'.1$ ). The candidate list includes:

1. all components from the  $\theta = 3''$  image with local signal-to-noise ratio  $\text{SNR} \equiv S_p^L/\sigma \geq 4$ , plus
2. a small number of additional components with  $\text{SNR} \equiv S_p^H/\sigma \geq 5$  from the  $\theta = 0''.66$  image.

For each of the candidate sources (item 1 above) the  $\theta = 0''.66$  catalog was searched for nearby components with  $S_p^H \geq 3 \mu\text{Jy beam}^{-1} \approx 3\sigma$ . An IR counterpart of each of the candidate sources was sought as described in Section 5.

From the candidate list, we kept as source components only:

1. the complete sample of 596 candidates with  $\text{SNR} \geq 5$  on the  $\theta = 3''$  image, plus

2. the reliable but incomplete sample of 156 candidates with  $4 \leq \text{SNR} < 5$  from the  $\theta = 3''$  image that were confirmed by an  $S_p^H \gtrsim 3\sigma$  component lying within  $3''$  on the  $\theta = 0''.66$  image. (Excluding regions blocked by the bright IR sources, 88% of these also were within  $1''.5$  of an IR source.) Plus
3. the additional 40 candidates with  $4 \leq \text{SNR} < 5$  from the  $\theta = 3''$  image that were confirmed only by an IR source lying within  $1''.5$  (see below).

Our final catalog contains 792 radio source components, a sample of which is shown in Table 2; the full table is available online. At  $\mu\text{Jy}$  levels there are very few resolved double radio sources, so nearly every cataloged radio source component is also a complete astrophysical radio source, defined as all of the radio emission from a single galaxy or AGN. Of the 209 source candidates from the  $\theta = 3''$  image with  $4 \leq \text{SNR} < 5$  and in locations where an IR identification was possible, only 14 had neither an IR identification nor a radio counterpart on the  $\theta = 0''.66$  image. 75% of these (154/205) were within  $1''.5$  of an IR source and outside of areas blocked by the brighter IR sources (see below).

## 5. Radio/IR Identifications

Most of our cataloged radio sources are powered by star-forming galaxies and AGNs that should be visible in sensitive IR images. Deep  $\lambda = 3.6\ \mu\text{m}$  and  $\lambda = 4.5\ \mu\text{m}$  images from the Spitzer Extragalactic Representative Volume Survey (SERVS) (Mauduit et al. 2012) cover the entire area we imaged at S-band, although part of the overlapping IR image is blinded by scattered light from the very bright star GX UMa at J2000  $\alpha = 10^{\text{h}} 46^{\text{m}} 07^{\text{s}}.70$ ,  $\delta = +59^{\circ} 03' 39''.2$ . Furthermore, the Mauduit et al. (2012) IR catalog excludes small regions around moderately bright foreground stars in which galaxies are still visible. We excluded from our radio/IR comparisons only the 48 sources in regions that are actually blinded by bright stars and kept as identification candidates all visible IR galaxies that had been excluded from the Mauduit et al. (2012) catalog. At both  $\lambda = 3.6\ \mu\text{m}$  and  $\lambda = 4.5\ \mu\text{m}$  the Mauduit et al. (2012) catalog  $5\sigma$  point-source detection limit is

$S \approx 2\ \mu\text{Jy}$  and the IR images have FWHM resolution  $\theta \approx 2''$ . The *Spitzer*  $\lambda = 4.5\ \mu\text{m}$  image in Figure 2 shows that nearly all of our radio source positions (crosses) have IR identifications.

We identified *Spitzer* IR sources with radio sources in Table 2 on the basis of position coincidence: the IR source nearest to the radio source was accepted as the identification if it lies within our maximum search radius  $r_s$ . The probability that an unrelated IR source will incorrectly be identified depends on the radio and IR position uncertainties and on the sky density  $\rho$  of IR identification candidates. The left panel of Figure 1 shows a histogram of radial distances  $r$  to the IR sources nearest to an arbitrary grid of  $120 \times 120 = 14400$  positions spaced by  $10''$  in right ascension and declination. The histogram is well approximated by the expected Rayleigh distribution

$$P(r) = \frac{r}{\sigma^2} \exp\left(-\frac{r^2}{2\sigma^2}\right) = 2\pi\rho r \exp(-\pi\rho r^2), \quad (4)$$

where  $\sigma \approx 3''.35$  is the fitted rms width of the distribution and  $\rho = (2\pi\sigma^2)^{-1} \approx 0.0142\ \text{arcsec}^{-2}$  is the implied sky density of IR sources.

This result can be used to calculate how strongly having IR companions within  $1''.5$  confirms the reality of the 40 faint ( $4 \leq \text{SNR} < 5$ ) sources found only on the  $\theta = 3''$  radio image. The cumulative Rayleigh distribution

$$P(< r) = 1 - \exp\left(-\frac{r^2}{2\sigma^2}\right) \quad (5)$$

specifies the probability that an unrelated IR source lies within a distance  $r$  from any point on the sky. For  $\sigma = 3''.35$ , the probability that a spurious radio source would have an IR companion within  $1''.5$  is  $P(< 1''.5) \approx 0.095$ , so an IR confirmation boosts the reliability of a  $4 \leq \text{SNR} < 5$  radio source by a factor of  $0.095^{-1} \sim 10$ .

The offsets  $r$  of most genuine radio/IR identifications should have a roughly Rayleigh distribution whose rms is the quadratic sum of the radio position error, the IR position error, and any radio-IR offset intrinsic to the host galaxy. The distribution of IR offsets from the radio positions of the 752 radio sources *not* confirmed only by an IR source lying within  $1''.5$  is shown by the histogram in the right panel of Figure 1, and the continuous curve fitting most sources is a Rayleigh

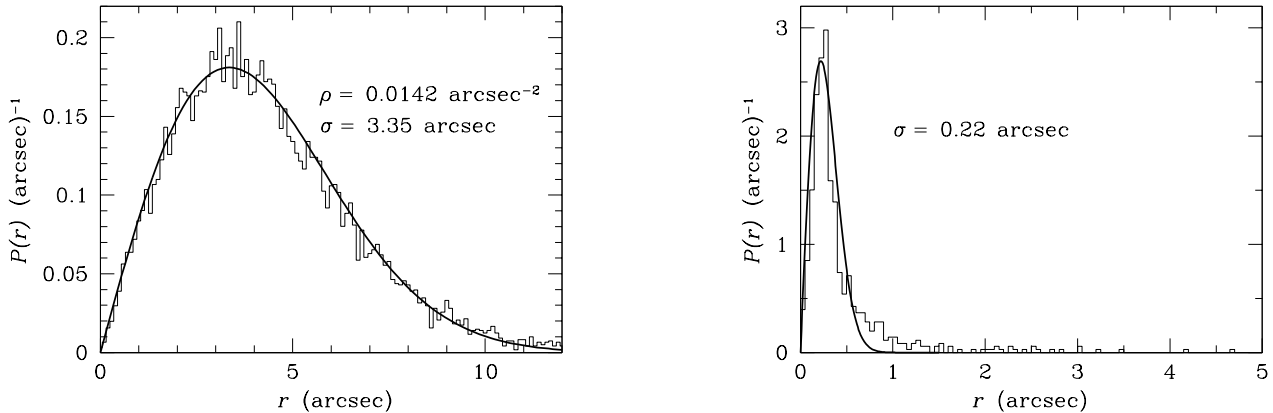


Fig. 1.— Left panel: Histogram of measured radial offsets  $r$  between points on an arbitrary grid of  $120 \times 120$  positions separated by  $10''$  and their nearest IR neighbors. The data are well fit by the Rayleigh distribution (smooth curve) with rms  $\sigma = 3''.35$ , expected for randomly scattered IR sources with mean sky density  $\rho = 0.0142 \text{ arcsec}^{-2}$ . Right panel: Histogram of measured radial separations  $r$  between radio sources in Table 2 (excluding the IR-blinded fields and the faint sources kept only because they have IR counterparts within  $1''.5$ ) and their nearest IR neighbors. The core of this distribution can be approximated by a Rayleigh distribution with rms  $\sigma \approx 0''.22$ , but there is a tail of somewhat larger offsets, many of which are genuine radio-IR matches. Abscissae: Angular distance (arcsec) between a radio source and its nearest IR neighbor. Ordinates: Probability density ( $\text{arcsec}^{-1}$ ).

Table 1: Observations.

| Array | Date Range           | Time | No. |
|-------|----------------------|------|-----|
| C     | 2012 Feb 21 – Mar 18 | 57.0 | 6   |
| B+    | 2014 Feb 02 – Feb 18 | 26.0 | 10  |
| A     | 2015 Jul 10 – Sep 13 | 39.4 | 6   |

“Array” is the VLA configuration. The start and end dates give the period over which the data were taken. “Time” is the total observing time in hours, and “No.” is the number of separate observing sessions. The “C” observations used the array prior to fully outfitting with 3 GHz receivers and included only 21 antennas.

distribution with  $\sigma \approx 0''.22$ . However, there is a tail of sources with offsets too large to be consistent with this Rayleigh distribution yet too small to be explained by the Rayleigh distribution of unrelated sources shown in the left panel. Such tails are not rare (e.g., Murphy et al. 2017) and can be attributed to a few sources with larger combined position errors, extended galaxies with genuine IR-radio offsets, sources in clusters and a small contamination by unrelated IR sources.

To determine the optimum search radius  $r_s$  that will accept most genuine identifications and minimize contamination by unrelated IR sources, we exploited the fact that all unrelated sources should obey the Rayleigh offset distribution with  $\sigma = 3''.35$  shown in the left panel of Figure 1. The fraction of background sources with  $r > \sigma = 3''.35$  is  $P(> r) = 1 - P(< r) \approx 0.606$ . On the conservative assumption that all 10 sources with  $r > \sigma = 3''.35$  in our catalog are unrelated to their IR neighbors, the total number of unrelated IR sources with *any*  $r > 0$  should be  $N_u \approx (10 \pm 3)/0.606 \approx 16.5 \pm 5$ . Excluding the 40 faint sources cataloged only because they have IR identifications and the 48 unidentifiable sources in regions overwhelmed by bright IR stars, Table 2 contains an IR-unbiased sample of 704 radio sources

TABLE 2  
SOURCE CATALOG.

| J2000 $\alpha$ |    |                | J2000 $\delta$ |    | $\theta$     | $g_0$ | $S_p^L$                      | $S^L$              | L-H          | $S_p^H$                      | $S^H$              | $\phi$       | $r$      |      |
|----------------|----|----------------|----------------|----|--------------|-------|------------------------------|--------------------|--------------|------------------------------|--------------------|--------------|----------|------|
| h              | m  | s              | °              | m  | ''           |       | ( $\mu\text{Jy beam}^{-1}$ ) | ( $\mu\text{Jy}$ ) | ( $''$ )     | ( $\mu\text{Jy beam}^{-1}$ ) | ( $\mu\text{Jy}$ ) | ( $''$ )     | ( $''$ ) |      |
| 10             | 44 | 43.071 ± 0.071 | 58             | 59 | 51.05 ± 0.55 | L     | 0.26                         | 19.49 ± 3.98       | 25.70 ± 5.76 | 4.53                         |                    |              | 1.10     |      |
| 10             | 44 | 44.109 ± 0.009 | 59             | 00 | 19.36 ± 0.07 | H     | 0.27                         | 16.96 ± 4.02       | 16.00 ± 3.82 | 0.20                         | 21.18 ± 3.31       | 20.66 ± 3.29 | < 0.61   | 0.24 |
| 10             | 44 | 46.577 ± 0.015 | 58             | 58 | 40.70 ± 0.11 | H     | 0.28                         | 14.96 ± 3.66       | 14.06 ± 3.47 | 0.35                         | 12.07 ± 3.30       | 11.17 ± 3.07 | < 0.86   | 0.24 |
| 10             | 44 | 46.940 ± 0.007 | 59             | 01 | 56.37 ± 0.04 | H     | 0.30                         | 39.90 ± 3.46       | 44.51 ± 4.26 | 0.13                         | 33.50 ± 3.01       | 33.23 ± 3.15 | < 0.45   | 0.50 |
| 10             | 44 | 47.417 ± 0.013 | 58             | 58 | 01.79 ± 0.10 | H     | 0.27                         | 18.33 ± 3.76       | 17.56 ± 3.64 | 0.23                         | 13.59 ± 3.25       | 12.82 ± 3.09 | < 0.79   | 0.18 |
| 10             | 44 | 47.563 ± 0.006 | 58             | 59 | 18.74 ± 0.03 | H     | 0.30                         | 49.70 ± 3.60       | 49.44 ± 3.88 | 0.13                         | 55.51 ± 3.04       | 55.34 ± 3.45 | < 0.36   | 0.29 |
| 10             | 44 | 47.661 ± 0.005 | 59             | 00 | 35.66 ± 0.03 | H     | 0.31                         | 88.76 ± 3.61       | 91.48 ± 4.67 | 0.06                         | 79.23 ± 3.02       | 80.61 ± 3.93 | < 0.33   | 0.38 |
| 10             | 44 | 47.725 ± 0.018 | 59             | 02 | 14.60 ± 0.14 | H     | 0.31                         | 34.85 ± 3.39       | 35.53 ± 3.66 | 0.82                         | 11.34 ± 3.04       | 12.69 ± 3.66 | < 1.15   | 0.83 |
| 10             | 44 | 47.794 ± 0.012 | 58             | 58 | 12.47 ± 0.08 | H     | 0.28                         | 19.53 ± 3.69       | 19.97 ± 3.93 | 0.54                         | 15.82 ± 3.22       | 15.16 ± 3.12 | < 0.72   | 0.77 |
| 10             | 44 | 49.188 ± 0.014 | 58             | 57 | 19.82 ± 0.10 | H     | 0.27                         | 17.85 ± 3.82       | 17.04 ± 3.68 | 0.65                         | 12.71 ± 3.28       | 11.86 ± 3.08 | < 0.83   | 0.47 |

∞

NOTE.—Table 2 is published in its entirety in machine-readable format. A portion is shown here for guidance regarding its form and content. The table lists J2000 right ascensions  $\alpha$  and declinations  $\delta$  measured from the  $\theta = 0''.66$  resolution image if available (indicated by “H” in the  $\theta$  column), otherwise from the  $\theta = 3''$  resolution image (“L” in the  $\theta$  column). Interpretation of the fitted Gaussian parameters follows the development in (Condon 1997). The rms position errors include our estimated absolute astrometric uncertainty  $\sigma_\alpha = \sigma_\delta \approx 0''.02$ . Column  $g_0$  gives the normalized antenna gain at the source position. The 3 GHz peak and total flux densities corrected for fitting bias (Condon (1997)) from the low-resolution image are listed under  $S_p^L$  and  $S^L$ . L-H is the separation of the positions measured on the low- and high-resolution images.  $S_p^H$  and  $S^H$  are the peak and integrated flux densities from the high-resolution image. Column  $\phi$  gives the deconvolved Gaussian source FWHM sizes or upper limits at  $0''.66$  resolution. Next,  $r$  is the angular distance between the radio source and its nearest IR neighbor. Separations less than  $1''.5$  are considered solid associations,  $1''.5 \leq r \leq 3''.5$  are probable associations, and  $r > 3''.5$  are unassociated.

of which  $\approx (704 - 16.5)/704 = 97.7 \pm 0.8\%$  have true IR identifications stronger than  $S \approx 2 \mu\text{Jy}$  at  $\lambda = 4.5 \mu\text{m}$ . This high radio/IR identification rate also indicates that  $\lesssim 2\%$  of the cataloged radio sources can be spurious.

The expected numbers of background sources in different ranges of  $r$  can be calculated from Equation 5 and compared with the observed numbers plotted in the right panel of Figure 1 to estimate the reliability  $R$  of an identification as a function of  $r$ , as shown in Table 3. For  $r < 1''$ ,  $R \approx 1$ . In the range  $1'' < r < 1''.5$ , the average number of unrelated background sources  $\langle N_u \rangle \approx 0.85$  is much smaller than the observed number  $N_o = 23$  of radio/IR matches, suggesting that  $R \approx (N_o - \langle N_u \rangle)/N_o \approx 0.96$ . Thus a search radius  $r_s = 1''.5$  should yield highly reliable radio/IR identifications. Table 3 shows how reliability decreases for larger separations. Nevertheless, more than half of the ‘‘probable’’ identifications with  $1''.5 < r < 3''.5$  appear to be correct.

Let  $m \equiv r_s/\sigma$  be the search radius in units of the rms position error  $\sigma \approx 0''.22$  and define  $k \equiv 1 + 2\pi\rho\sigma^2 \approx 1.0043$ . Then the completeness  $C$  of our position-coincidence identifications is

$$C = \frac{1 - \exp(-m^2 k/2)}{k} \approx 0.996 \quad (6)$$

and the reliability  $R$  is

$$R = C \left[ \frac{1}{f} - \left(1 - \frac{1}{f}\right) \exp[m^2(1 - k)/2] - \exp\left(-\frac{m^2 k}{2}\right) \right]^{-1} \approx 0.957 \quad (7)$$

(Condon et al. 1975).

Table 3: IR identification reliability.  $R$

| $r''$   | $\langle N_u \rangle$ | $N_o$ | $R$  |
|---------|-----------------------|-------|------|
| 1.0–1.5 | 0.85                  | 23    | 0.96 |
| 1.5–2.0 | 1.12                  | 8     | 0.86 |
| 2.0–2.5 | 1.32                  | 9     | 0.85 |
| 2.5–3.0 | 1.44                  | 5     | 0.71 |
| 3.0–3.5 | 1.49                  | 4     | 0.63 |

Notes: For each radio-IR offset range  $r$ ,  $\langle N_u \rangle$  is the average number of unrelated IR sources,  $N_o$  is the observed number of IR sources, and  $R$  is the estimated identification reliability.

## 6. Source Size Distribution

Most of the individual fitted Gaussian sizes produced in the source-finding process are sufficiently uncertain to yield only upper limits to the individual deconvolved source sizes. However, the mean ratio  $\langle S_p^H/S_p^L \rangle$  of the fitted peak brightness  $S_p^H$  (on the  $\theta_H = 0''.66$  high-resolution image) to  $S_p^L$  (on the  $\theta_L = 3''$  low-resolution image) depends on the source solid angle. If a circular Gaussian source of FWHM diameter  $\phi$  and flux density  $S$  is imaged with a beam of FWHM diameter  $\theta$ , the source appears on the image as a circular Gaussian with FWHM diameter  $(\theta^2 + \phi^2)^{1/2}$  and peak brightness

$$S_p = S \left( \frac{\theta^2}{\theta^2 + \phi^2} \right). \quad (8)$$

If the circular Gaussian source is imaged with two different resolutions  $\theta_H$  and  $\theta_L$ , the ratio of the image peak brightnesses is

$$\frac{S_p^H}{S_p^L} = \left(1 + \frac{\phi^2}{\theta_L^2}\right) \left(1 + \frac{\phi^2}{\theta_H^2}\right)^{-1}. \quad (9)$$

Appendix C of Murphy et al. (2017) gives the  $S_p^H/S_p^L$  ratio for a source with the exponential brightness profile typical of spiral galaxies. Equation 9 can be solved for the source size  $\phi$ :

$$\phi = \left[ \frac{\theta_L^2 \theta_H^2 (S_p^L - S_p^H)}{\theta_L^2 S_p^H - \theta_H^2 S_p^L} \right]^{1/2}. \quad (10)$$

Even if a source does not have a circular Gaussian brightness distribution, Equation 10 defines what we call its equivalent source circular Gaussian FWHM.

Equations 9 and 10 allow us to estimate the statistical properties of the source sizes in our sample. The distribution of  $S_p^H/S_p^L$  as a function of  $S_p^L$  is given in Figure 3. Sources with and without IR counterparts are shown by different symbols. Horizontal lines give the expected values for circular Gaussians of various FWHM diameters  $\phi$ .

The cataloged sources were separated into peak brightness bins in which the bin-averaged peak brightnesses and peak brightness ratios are plotted in Figure 3 with ‘‘error bars’’ giving the rms ratio for the population in each bin. The peak brightness bin statistics are given in Table 4. Outliers further from the initial mean by more than

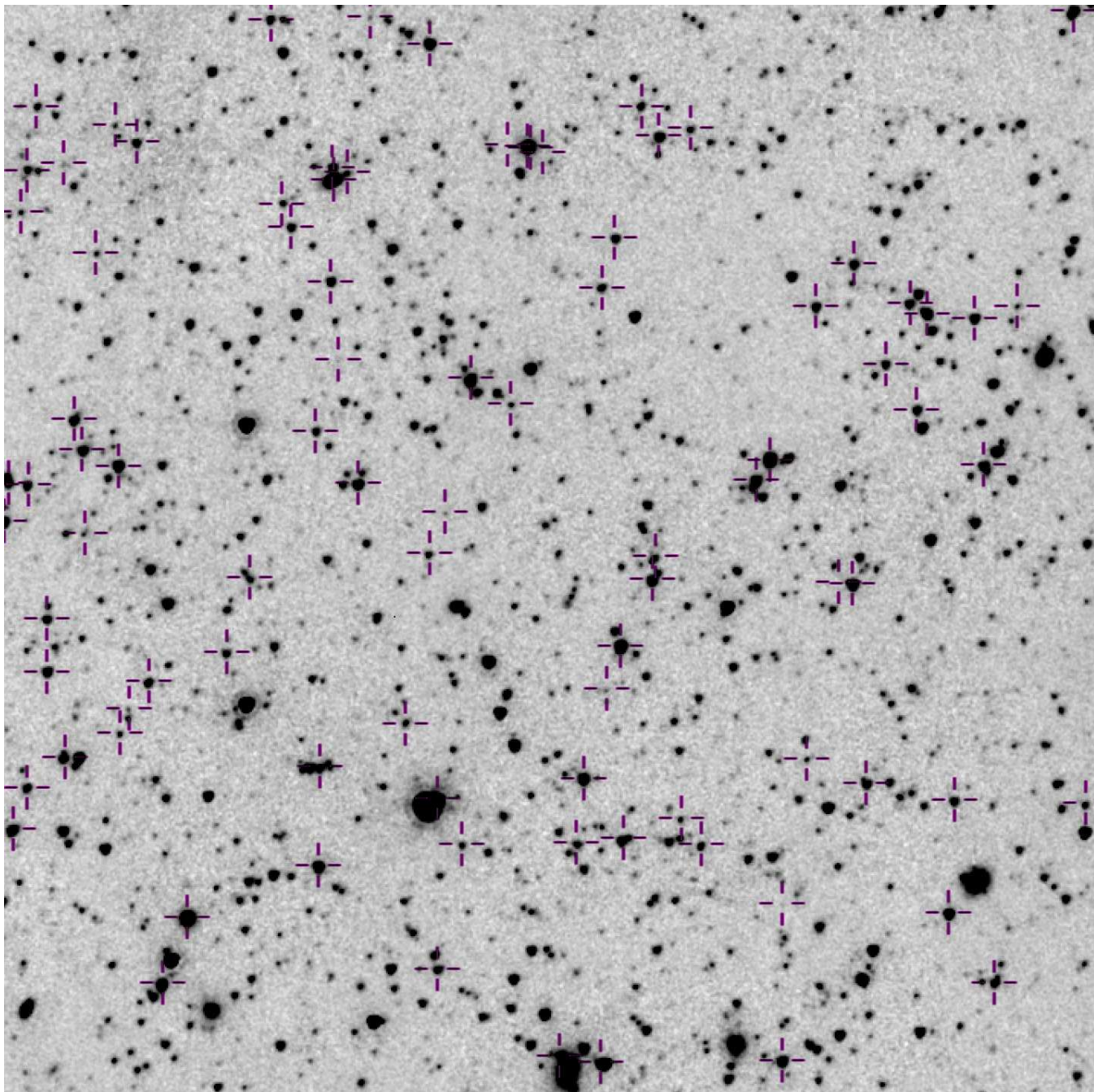


Fig. 2.— Radio positions marked by crosses on negative gray scale of the  $\lambda = 4.5 \mu\text{m}$  *Spitzer* image. The area shown is  $7'.2 \times 7'.0$ , with north up and east to the left; this is only a portion of the field imaged.

$2\sigma$  were excluded from the analysis of bin populations.

At peak brightnesses below the  $20\text{--}30\ \mu\text{Jy beam}^{-1}$  bin, the distribution of peak brightness ratios appears truncated on the low end by limited sensitivity. The  $20\text{--}30\ \mu\text{Jy beam}^{-1}$  and higher peak brightness bins in Table 4 consistently give an equivalent source circular Gaussian FWHM of  $\theta \approx 0''.3$ .

Figure 3 shows that the detected sources are generally marginally resolved at  $0''.66$  resolution. A more sensitive (although biased) estimate of the source size is the ratio of the peak brightness to the estimated integrated flux density from only the  $0''.66$  data. The integrated flux density is the Gaussian peak times the ratio of the fitted beam area to the CLEAN restoring beam area. Because the Gaussian fits were constrained to give a fitted beam no smaller than the CLEAN restoring beam, this estimate will be biased for point, or nearly unresolved sources. The plot of peak brightness to integrated flux densities is shown in Figure 4.

## 7. Completeness

The completeness of the sample of sources selected at  $3''$  resolution given in Table 2 was evaluated using a comparison with the  $8''$  resolution image of Condon et al. (2012). A catalog of sources generated from the  $8''$  resolution image was cross-matched with the catalog generated from the  $3''$  resolution image. Out of the 503  $8''$  resolution entries stronger than  $5\sigma$ , eight did not have matches at  $3''$  resolution. Of these, four were extended lobes of nearby bright sources, plausibly undetected at  $3''$  resolution, and one was in the masked region of the  $3''$  image. This suggests that the sample given in Table 2 is  $\approx 98.5\%$  complete. The ratios of the peak flux densities at  $3''$  to  $8''$  resolution for this sample are given in Figure 5. The analysis displayed in Figure 5 suggests a larger “typical” source size ( $\sim 1''.0$ ) than Figure 3, but this is a relatively small fraction of the  $3''$  resolution. The confusion “noise” in the  $8''$  image will also bias the flux density ratio lower, especially at the low flux densities.

Of the 792 entries in Table 2, 732 were detected in the  $0''.66$  image at  $\text{SNR} > 3$  while 60 were not. Thus, the high-resolution images have a 92% detection rate of the  $3''$  resolution sources, or approx-

imately 91% of sources detectable at  $8''$  resolution. The sources that were not detected at  $0''.66$  resolution are among the weakest in the sample.

The completeness as a function of the flux density is a function of the local image rms and thus a function of the antenna gain. Since only a single pointing was used, the noise is only (nearly) stationary in the image prior to correction for the antenna gain. The noise quoted in Table 2 was measured in a  $201 \times 201$  pixel box around each source, scaled by the inverse of the antenna gain. The average rms with and without antenna gain corrections as a function of distance from the pointing center for the  $0''.66$  image is shown in Figure 6.

## 8. Simulations

In order to estimate the effects of imaging and image analysis on the distribution of the apparent sizes of sources, simulated point and  $0''.5$  circular Gaussian sources with a range of flux densities were added to the visibility data sets. These were then imaged and the response in the derived image measured. In each of several simulations 144 artificial sources of a given size were added in a hexagonal grid; the location of the grid did not take into account the locations of real sources. The distributions of point and  $0''.5$  FWHM Gaussians are shown in Figure 7.

The simulated measurements tend to scatter around the expected ratio, although with less dispersion than seen in the actual source population in Figure 3. Outliers at the higher flux densities appear when the artificial source is located near a real source and the two are blended at  $3''$  resolution. Bin averages and rms values of the populations are shown in Figure 7 and are given in Table 5. Outliers further from the initial mean by more than  $2\sigma$  were excluded from the analysis of bin populations. Table 5 suggests that our analysis may statistically underestimate the sizes of the faintest sources. This effect is possibly the result of the bias in the Gaussian fitting of the high-resolution image towards the peak in the source plus noise, which will bias the derived peak brightness high.

A comparison between real and simulated sources of the statistics for the ratio  $S_p^H/S_p^L$  (for sources strong enough that the distribution is not truncated by sensitivity) can help constrain the

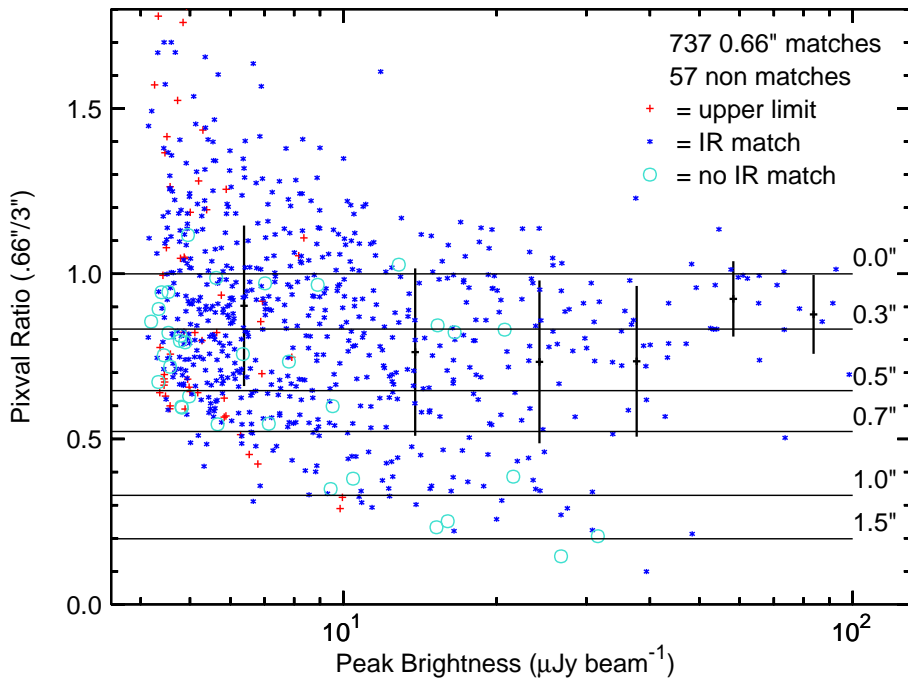


Fig. 3.— Distribution of  $S_p^H/S_p^L$  as a function of  $S_p^L$  peak brightness. Blue asterisks represent sources with IR matches within  $1''.5$ , cyan circles are sources with no IR match and small red pluses are  $3\sigma$  upper limits for sources not detected at  $0''.66$  resolution. Extended vertical bars are peak brightness-bin averaged values with the vertical extent showing the rms scatter  $\sigma_{\text{pop}}$  within the population. Horizontal solid lines mark the expected ratio of circular Gaussians with FWHM of the labeled size. Outliers are excluded from the bin statistics. The large number of points with a ratio in excess of 1.0 at low peak brightness is consistent with the noise.

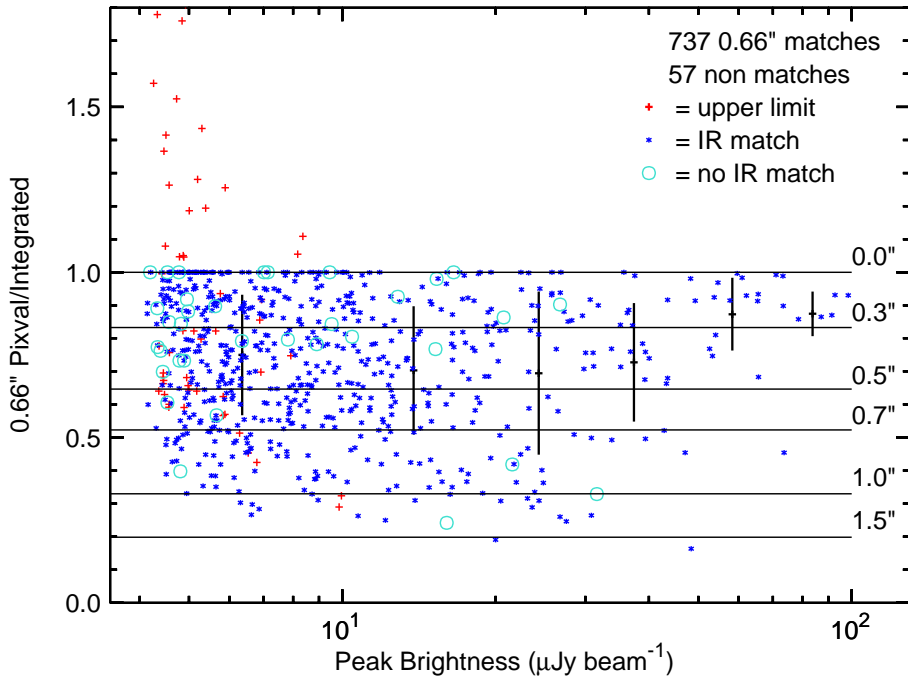


Fig. 4.— Like Figure 3, but for the ratio  $S_p^H/S^H$  versus peak brightness  $S_p^H$  in the  $0''.66$  resolution image. Red plus symbols are for sources not detected at  $0''.66$  resolution, where the ratio is the  $3\sigma$  upper limit to the  $3''$  peak brightness and the flux density is the peak brightness at  $3''$  resolution. The plotted ratio is equivalent to the ratio of the fitted beam area to the restoring beam area; fitting constraints limit this to a ratio of 1.0. The lowest peak brightness bin is biased low with respect to Figure 3 but the higher peak brightness bin averages are comparable in spite of being derived solely from the  $0''.66$  data.

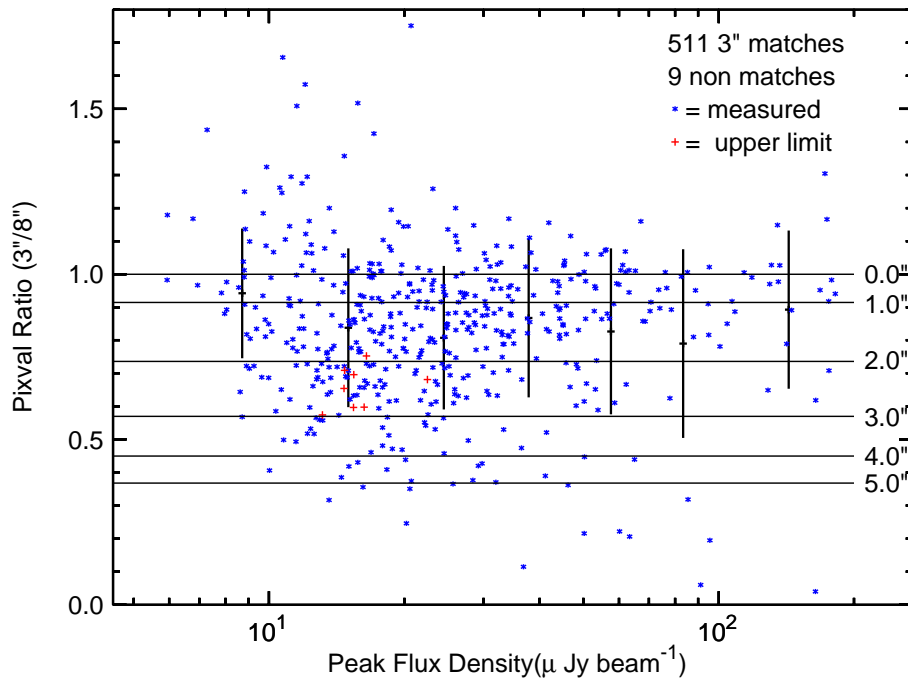


Fig. 5.— Like Figure 3, but for the ratio of the peak brightness at 3'' resolution to that at 8'' resolution versus the 8'' peak brightness. All but nine of the 8'' resolution sample were detected, but the peak brightness are systematically below 1.0.

Table 4: Measured average ratios of peak flux densities.

| No. | $\langle S_p^L \rangle$<br>$\mu\text{Jy}$ | $\langle S_p^H/S_p^L \rangle$ | $\sigma_{\text{pop}}$ | FWHM<br>" | err<br>" |
|-----|---|-------------------------------|-----------------------|-----------|----------|
| 428 | 6.4                                       | 0.76                          | 0.18                  | 0.39      | 0.19     |
| 165 | 13.9                                      | 0.71                          | 0.19                  | 0.43      | 0.21     |
| 52  | 24.3                                      | 0.69                          | 0.25                  | 0.45      | 0.27     |
| 31  | 37.4                                      | 0.77                          | 0.18                  | 0.38      | 0.19     |
| 14  | 58.3                                      | 0.87                          | 0.11                  | 0.26      | 0.13     |
| 9   | 83.8                                      | 0.93                          | 0.07                  | 0.20      | 0.09     |

Notes: “No.” is the number of sources in the bin, excluding outliers,  $\langle S_p^L \rangle$  is the average peak brightness at 3" resolution,  $\langle S_p^H/S_p^L \rangle$  is the average peak brightness ratio,  $\sigma_{\text{pop}}$  is the rms ratio of the bin sample, “FWHM” is the equivalent half-power diameter of a circular Gaussian with the ratio of the bin average, and “err” is the estimated 1  $\sigma$  error of “FWHM”.

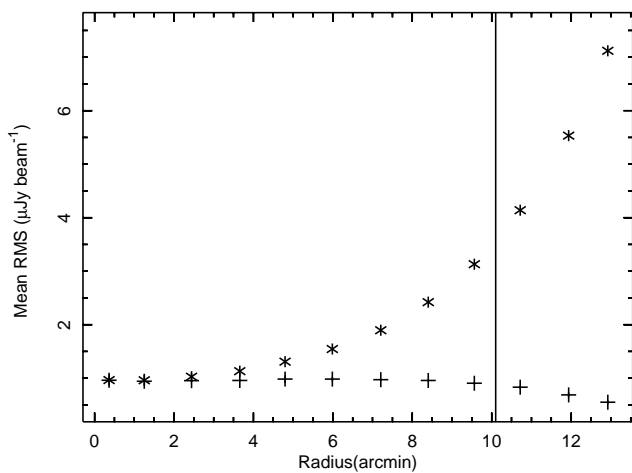


Fig. 6.— Average source rms in the 0".66 image as a function of distance from the pointing center. Plus symbols indicate the values without antenna gain correction, while asterisks are after correction. The vertical line indicates the maximum distance from which sources were included in Table 2.

Table 5: Simulation flux bin ratio averages.

| No. | $\phi$<br>" | $\langle S_p^L \rangle$<br>$\mu\text{Jy}$ | $\langle S_p^H/S_p^L \rangle$ | $\sigma_{\text{pop}}$ | FWHM<br>" | err<br>" |
|-----|-------------|---|-------------------------------|-----------------------|-----------|----------|
| 27  | 0.0         | 4.4                                       | 0.91                          | 0.25                  | 0.21      | 0.33     |
| 36  | 0.0         | 6.5                                       | 1.07                          | 0.23                  | 0.00      | 24.6     |
| 16  | 0.0         | 7.9                                       | 1.02                          | 0.24                  | 0.00      | 25.7     |
| 36  | 0.0         | 14.5                                      | 0.93                          | 0.18                  | 0.19      | 0.26     |
| 36  | 0.0         | 16.4                                      | 0.99                          | 0.08                  | 0.08      | 0.26     |
| 17  | 0.0         | 18.0                                      | 0.98                          | 0.08                  | 0.11      | 0.18     |
| 36  | 0.5         | 4.9                                       | 0.74                          | 0.28                  | 0.40      | 0.29     |
| 88  | 0.5         | 6.7                                       | 0.72                          | 0.21                  | 0.43      | 0.23     |
| 89  | 0.5         | 9.2                                       | 0.69                          | 0.14                  | 0.46      | 0.15     |
| 25  | 0.5         | 17.1                                      | 0.66                          | 0.09                  | 0.49      | 0.10     |
| 85  | 0.5         | 19.6                                      | 0.68                          | 0.06                  | 0.47      | 0.07     |
| 26  | 0.5         | 22.0                                      | 0.65                          | 0.05                  | 0.50      | 0.06     |

Notes: “No.” is the number of simulated sources in the bin, excluding outliers. The column labeled  $\phi$  in Table 5 gives the FWHM of the simulated source, while “FWHM” gives the equivalent circular Gaussian half-power diameter corresponding to the bin average ratio, and “err” is the estimated 1  $\sigma$  error of “FWHM”.

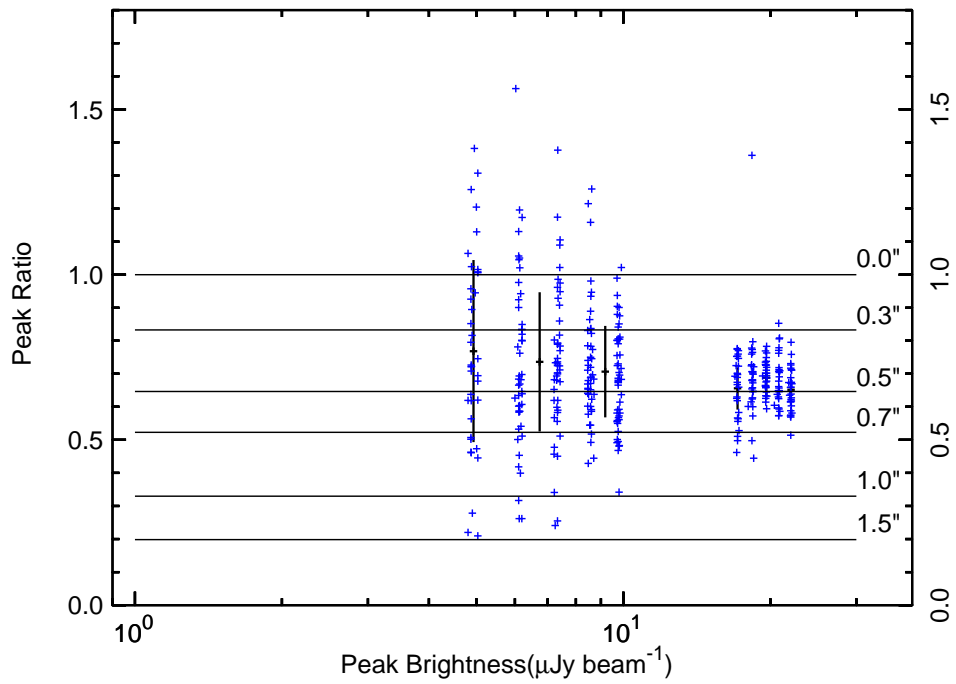
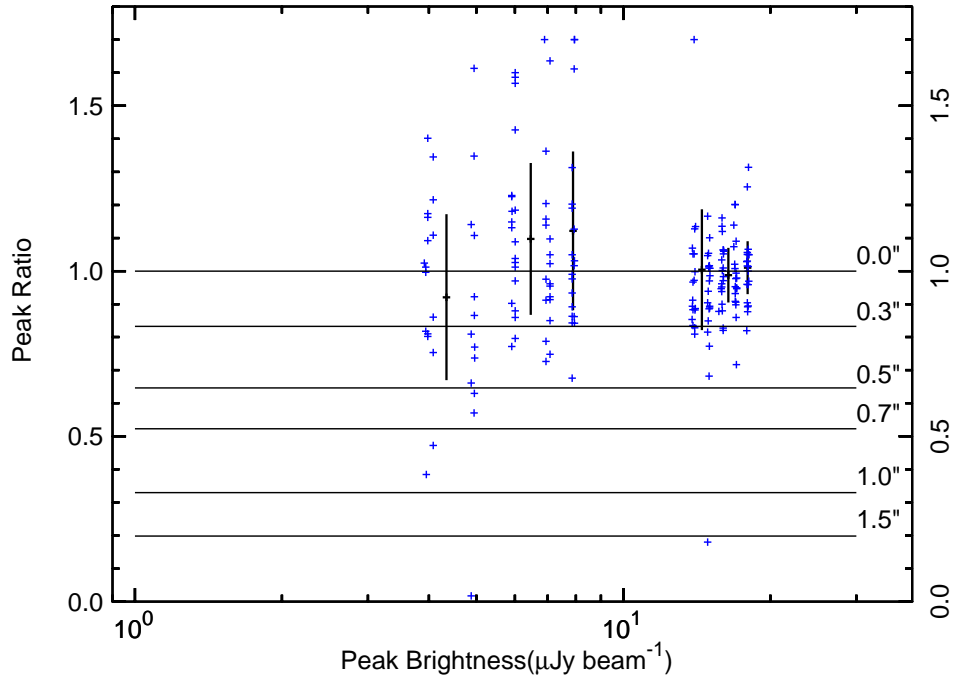


Fig. 7.— Like Figure 3, but for artificial sources added to the data and imaged. The abscissa is the model  $S_p^L$ . The upper plot has point sources, while the lower has circular Gaussians of 0.5" FWHM. Bin averages and rms deviations of the population are shown by the black vertical bars.

range of source effective sizes. The simulated source results will include all of the noise and image processing artifacts suffered by the real sources, except for calibration and antenna pointing errors. The bulk of the sources not detected at the higher resolution are at the lower flux densities and are likely not detected due to sensitivity. The following is a general analysis of the source population at these flux density levels.

The real sources in the well-sampled range of  $10\text{--}50 \mu\text{Jy beam}^{-1}$  have a typical population rms  $\sigma_{\text{pop}} = 0.26$  in this ratio (Table 4). The simulated sources in Table 5 typically have  $\sigma_{\text{pop}} = 0.10$  in this peak brightness range for both point and  $0''.5$  circular Gaussians. The expected ratio for a  $0''.5$  Gaussian is  $S_p^{\text{H}}/S_p^{\text{L}} = 0.65$  and for a point source is  $S_p^{\text{H}}/S_p^{\text{L}} = 1.0$ . The difference between the real and simulated source samples is that a range of sizes is expected for the real sources, whereas the simulations used only a single source size. The difference in the scatter of the peak brightness ratios between real and simulated sources is consistent with this expectation.

Thus the scatter in  $S_p^{\text{H}}/S_p^{\text{L}}$  is significantly less than the difference between an unresolved and a  $0''.5$  source. This means that the real source size distribution must be relatively tightly clustered about the typical  $\phi \approx 0''.3$  equivalent circular Gaussian. Assuming the measured  $\sigma_{\text{pop}}$  values are the rms scatter of a Gaussian distributed population, a simple analysis of the ratio statistics gives a distribution with a mean value of  $\langle\phi\rangle = 0''.3 \pm 0''.1$  and an rms scatter  $\lesssim 0''.3$  of the distribution.

## 9. FIR/radio correlation

The positions of radio sources in Table 2 brighter than  $5\sigma$  were examined in deep *Herschel*  $\lambda = 160 \mu\text{m}$  images (Oliver et al. 2012). The *Herschel* image is confusion limited, so only sources brighter than 5 times the  $0.4 \mu\text{Jy pixel}^{-1}$  rms noise were considered real. Aperture photometry was performed on the  $160 \mu\text{m}$  image by summing all pixels within a radius of three pixels and multiplying by 1.195. This correction factor was derived by a comparison on the brightest source in the field with a much larger aperture. The results are shown in Figure 8, with upper limits indicated by the hatched areas. The bulk of the sources with  $160 \mu\text{m}$  detections are within a fairly narrow

range of  $\log[\langle S(160 \mu\text{m})/S(3 \text{ GHz}) \rangle] = 2.3$  in the observer’s frame, or  $\log[\langle S(80 \mu\text{m})/S(1.5 \text{ GHz}) \rangle] = 2.3$  in the source frame at  $z \sim 1$ , indicating that most obey the FIR/radio correlation typical of star-forming galaxies.

## 10. Polarization

The A-configuration data were imaged in Stokes  $I$ ,  $Q$ , and  $U$ . Sources with polarized emission in excess of twice the polarized rms after bias correction are listed in Table 6. Three have FR I/II morphologies, but another three are either unresolved or marginally resolved. Few sources were bright enough that a 1% polarization could have been detected.

## 11. Extended Sources

Six sources are sufficiently complex that they are not adequately described by a superposition of Gaussian components. They all appear to be AGN-driven FR I and FR II sources. They are summarized in Table 7.

## 12. Discussion

The median size derived for the faint source population is consistent with that expected for a population dominated by star-forming galaxies. The “effective radius”  $r_e$  of a galaxy is the radius enclosing half the emitted radiation. For an exponential disk,  $r_e \approx \phi/2.43$  (Murphy et al. 2017), so our star-forming galaxies have  $\langle r_e \rangle \approx 0''.12 \approx 1 \text{ kpc}$  for  $z \sim 1$ . This is somewhat larger than the  $\langle r_e \rangle = 0''.069 \pm 0''.013$  reported by (Murphy et al. 2017), whose  $\nu = 10 \text{ GHz}$  sources have a larger thermal fraction and are less broadened by cosmic-ray diffusion, and which were selected from an image with higher resolution ( $\theta = 0''.22$ ). On the other hand, our effective radius agrees well with the stacked  $\text{H}\alpha$  emission-line effective radius for high-mass galaxies at  $z \sim 1.4$ , after it was corrected for dust extinction (Nelson et al. 2016).

The sources in this study have a slightly smaller median angular size than galaxies selected at submm wavelengths, for sizes measured with ALMA observations in the far-infrared or with the VLA at 3 GHz. Hodge et al. (2016) estimated a mean effective radius  $\langle r_e \rangle = 1.8 \pm 0.2 \text{ kpc}$  of dust emission at 345 GHz in 16 submm galax-

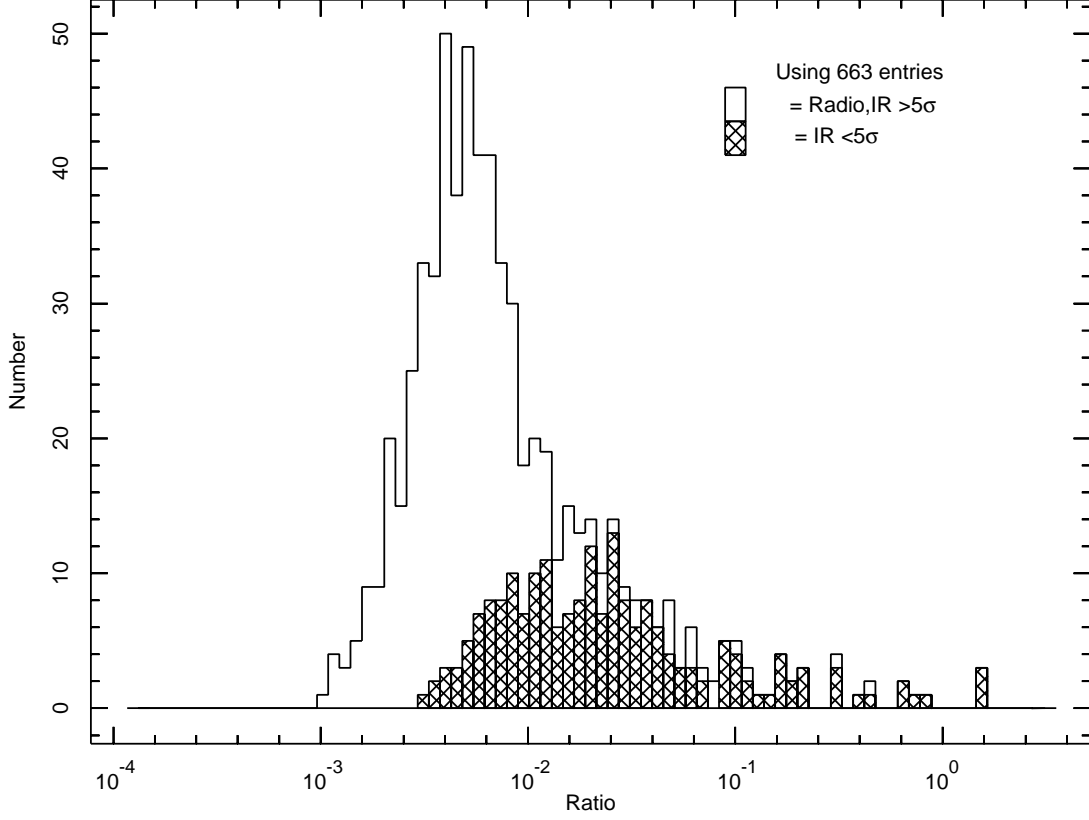


Fig. 8.— Histogram of the ratio of the 3 GHz flux density to the  $\lambda = 160 \mu\text{m}$  *Herschel* flux density for the sources in Table 2. Hatched areas indicate sources without a solid *Herschel* detection.

Table 6: Polarized sources

| J2000 $\alpha$ | J2000 $\delta$ | $I$<br>$\mu\text{Jy beam}^{-1}$ | $P$<br>$\mu\text{Jy beam}^{-1}$ | EVPA<br>$^{\circ}$ | Comment         |
|----------------|----------------|---------------------------------|---------------------------------|--------------------|-----------------|
| 10 45 25.972   | 58 58 45.06    | $8.3 \pm 0.9$                   | $3.7 \pm 1.7$                   | $+1.8 \pm 9.4$     | Weak, isolated  |
| 10 45 39.783   | 58 57 29.80    | $493 \pm 16$                    | $14.4 \pm 6.0$                  | $+5.1 \pm 4.4$     | Part of FR I    |
| 10 45 48.960   | 58 54 07.86    | $8.8 \pm 1.2$                   | $5.9 \pm 2.4$                   | $+89.8 \pm 8.3$    | Extended AGN    |
| 10 46 16.140   | 59 04 30.02    | $29.5 \pm 1.2$                  | $3.8 \pm 1.6$                   | $-38.9 \pm 8.4$    | Isolated, small |
| 10 46 23.967   | 59 06 10.12    | $178 \pm 7$                     | $30 \pm 9$                      | $-29.3 \pm 2.9$    | FR II N Lobe    |
| 10 46 24.494   | 59 04 48.44    | $73.7 \pm 4.0$                  | $9.3 \pm 3.0$                   | $-67.4 \pm 5.0$    | FR II S Lobe    |
| 10 46 24.847   | 59 04 45.97    | $3979 \pm 126$                  | $592 \pm 9$                     | $+0.1 \pm 0.1$     | FR II S Lobe    |
| 10 46 44.540   | 59 01 16.26    | $207 \pm 7$                     | $12.3 \pm 2.6$                  | $-18.1 \pm 3.7$    | Isolated, small |

Notes:  $I$  is the *Stokes*  $I$  peak flux density followed by its rms error,  $P$  is the polarized peak flux density ( $\sqrt{Q^2 + U^2}$ ) followed by its error, and  $EVPA$  is the electric field position angle measured east from north.

ies at  $\langle z \rangle \sim 2.5$ , and Simpson et al. (2015) found  $\langle r_e \rangle = 1.2 \pm 0.1$  kpc for 52 submm-selected galaxies, also at 345 GHz. Miettinen et al. (2017) reported a mean Gaussian FWHM size  $4.6 \pm 0.4$  kpc (corresponding to  $\langle r_e \rangle \approx 1.9$  kpc) at 3 GHz for a sample of 115 submm-selected galaxies detected in the COSMOS VLA radio survey (Smolčić et al. 2017). However, all three of these studies are dominated by submm-selected galaxies with significantly higher redshifts and star-formation rates than the radio-selected objects in this paper:  $\langle z \rangle \sim 2.5$  and  $\langle L_{\text{FIR}} \rangle \sim 4 \times 10^{12} L_{\odot}$  for the submm-selected galaxies, versus  $\langle z \rangle \sim 1$  and  $\langle L_{\text{FIR}} \rangle \sim 1 \times 10^{11} L_{\odot}$  for the faint radio sources discussed here. Thus the size differences are broadly consistent with an extrapolation of the  $r_e$ - $L_{\text{FIR}}$  relation of Fujimoto et al. (2017) to lower FIR luminosities.

### 13. Summary

A catalog of 792 radio sources at 3 GHz was derived from sensitive ( $\sigma \approx 1 \mu\text{Jy beam}^{-1}$ ) VLA S-band ( $2 < \nu < 4$  GHz) images having  $3''$  and  $0''.66$  resolution. The reliability of the source detections was evaluated and is supported by identifications with IR sources from the *Spitzer* observations described in Mauduit et al. (2012). Because 97.7% of the radio sources have IR counterparts, the reliability of sources in the catalog should be  $\gtrsim 98\%$ . The strong FIR/radio correlation between the flux densities the radio detections and their far IR counterparts shown in Figure 8 suggests that the radio sources are dominated by star formation. Polarized radio emission was detected in only six

source components.

The typical source size was estimated from the statistics of the ratio  $S_{\text{p}}^{\text{H}}/S_{\text{p}}^{\text{L}}$  of peak flux densities at  $0''.66$  and  $3''$  resolutions. 92% of the sources detected at the lower resolution were also detected in the high-resolution image. Most of the non-detections are at the lowest flux densities, hence likely due to resolution and limited brightness sensitivity. Both Figures 3 and 4, as well as Table 4, show that at peak sky flux densities high enough that the distribution is not truncated by sensitivity ( $\sim 20 \mu\text{Jy beam}^{-1}$ ) the distribution is centered on a ratio corresponding to a source with a circular Gaussian FWHM  $\langle \phi \rangle = 0''.3 \pm 0''.1$ . The scatter is larger than at corresponding flux densities of simulated point or  $0''.5$  FWHM sources, indicating a range of intrinsic source sizes, with a few completely resolved at the higher resolution. The rms scatter in the  $S_{\text{p}}^{\text{H}}/S_{\text{p}}^{\text{L}}$  ratios of real sources is less than the difference in the ratios expected for unresolved and circular Gaussians of  $0''.5$  FWHM; thus, the scatter about the typical size is fairly small. Table 5 gives the analysis for the simulated sources and suggests that the sizes are slightly underestimated. A simple analysis of the ratio statistics gives a distribution of the equivalent circular Gaussian FWHM, with a median  $\langle \phi \rangle = 0''.3 \pm 0''.1$  and a population size scatter  $\sigma_{\text{pop}} \lesssim 0''.3$ .

We thank the anonymous reviewer for the many comments and suggestions leading to a clearer description of these results. This work is based in part on observations made with the Spitzer Space Telescope, which is operated by the Jet Propulsion Laboratory, California Institute of Technology under a contract with NASA. This work is also based in part on observations made with Herschel, a European Space Agency Cornerstone Mission with significant participation by NASA. Herschel is an ESA space observatory with science instruments provided by European-led Principal Investigator consortia and with important participation from NASA.

*Facility:* VLA.

### REFERENCES

Bracewell, R. N. 2012, *Fourier Analysis and Imaging*, Springer Science & Business Media, p 413

Table 7: Extended Sources.

| J2000 $\alpha$ | J2000 $\delta$ | LAS  | $S$            |
|----------------|----------------|------|----------------|
|                |                | "    | $\mu\text{Jy}$ |
| 10 45 37.189   | 59 09 45.48    | 2.8  | 397            |
| 10 45 39.783   | 58 57 29.79    | 12.1 | 1877           |
| 10 45 49.226   | 58 54 12.59    | 6.7  | 392            |
| 10 46 24.005   | 59 05 22.29    | 86.4 | 8617           |
| 10 46 33.215   | 58 58 15.42    | 2.4  | 239            |
| 10 46 38.337   | 58 54 20.31    | 17.4 | 575            |

Notes: LAS is the largest angular size,  $S$  is the integrated flux density.

- Briggs, D. S. 1995, Ph. D. thesis, New Mexico Institute of Mining and Technology, Available <http://www.aoc.nrao.edu/ftp/dissertations/\dbriggs/diss.html>
- Condon, J. J. 1984, ApJ, 287, 461
- Condon, J. J. 1997, PASP, 109, 166
- Condon, J. J. 2007, ASPC, 380, 189
- Condon, J. J., Balonek, T. J., & Jauncey, D. L. 1975, AJ, 80, 887
- Condon, J. J., Cotton, W. D., Fomalont, E. B., Kellermann, K. I., Miller, N., Perley, R. A., Scott, D., Vernstrom, T., & Wall, J. V. 2012, ApJ, 758, 23
- Cotton, W. D. 2009, PASP, 120, 439
- Fujimoto, S., Ouchi, M., Shibuya, T., & Nagai, H. 2017, arXiv:1703.02138
- Heywood, I., Jarvis, M. J., & Condon, J. J. 2013, MNRAS, 423, 2625
- Hodge, J. A., Swinbank, A. M., Simpson, J. M., et al. 2016, ApJ, 833, 103
- Mauduit, J. C., Lacy, M., Farrah, D. et al., 2012, PASP, 124, 714
- Miettinen, O., Delvecchio, I., Smolčić, V., et al. 2017, A&A, 606, A17
- Murphy, E. J., Momjian, E., Condon, J. J., Chary, R.-R., Dickinson, M., Inami, H., Taylor, A. R., & Weiner, B. J. 2017, ApJ, 839, 35
- Nelson, E. J., van Dokkum, P. G., Momcheva, I. G., Brammer, G. B., Wuyts, S., Franx, M., Schreiber, N. M. F., Whitaker, K. E., & Skelton, R. 2016, ApJ, 817:L9
- Oliver, S. J., Bock, J., Alteri, B., et al., 2012, MNRAS, 424, 1614
- Owen, F. N., & Morrison, G. E. 2008, AJ, 136, 1889
- Perley, R. A. 2016, EVLA Memo 195
- Perley, R. A., & Butler, B. J. (2013A), ApJS, 204, 19
- Perley, R. A. & Butler, B. J. (2013B), ApJS, 206, 16
- Simpson, J. M., Smail, I., Swinbank, A. M., et al. 2015, ApJ, 799, 81
- Smolčić, V., Novak, M., Bondi, M., et al. 2017, A&A, 602, A1
- Strazzullo, V., Pannella, M., Owen, F. N. et al., 2010, ApJ, 714, 1305
- Vernstrom, T., Scott, D., Wall, J. V., Condon, J. J., Cotton, W. D., Fomalont, E. B., Kellermann, K. I., Miller, N. & Perley, R.A. 2014, MNRAS, 440, 327
- Vernstrom, T., Scott, D., Wall, J. V., Condon, J. J., Cotton, W. D., Fomalont, E. B., Kellermann, K. I., and Perley, R.A. 2016, MNRAS, 462, 2934
- Wilman, R. J., Miller, L., Jarvis, M. J. et al., 2008, MNRAS, 388, 1335